

Modeling Electrospinning of Nanofibers

T.A. Kowalewski, S. Barral and T. Kowalczyk

Abstract A fast discrete model for the simulations of thin charged jets produced during the electrospinning process is derived, based on an efficient implementation of the boundary element method for the computation of electrostatic interactions of the jet with itself and with the electrodes. Short-range electrostatic forces are evaluated with slender-body analytical approximations, whereas a hierarchical force evaluation algorithm is used for long-range interactions. Qualitative comparisons with experiments is discussed.

1 Motivation

Electrospinning is a simple and relatively inexpensive mean of producing nanofibers by solidification of a polymer solution stretched by an electric field. Such fibers find applications in a variety of areas, including wound dressing [4], drug or gene delivery vehicles [19], biosensors [16], fuel cell membranes and electronics [15]. Recently electrospinning has been revitalized and successfully applied to the production of nanofibrous scaffolds for tissue-engineering processes [2], which constitute one of its most promising application.

A conventional electrospinning setup consists of a spinneret with a metallic needle, a syringe pump, a high-voltage power supply and a grounded collector. A polymer solution is loaded into the syringe and driven through the needle at a steady and controllable feed rate by the pump, forming a droplet at the tip of the needle. A high voltage (typically up to 30 kV) is applied between the tip and a grounded collector. When the electric field strength overcomes the surface tension of the droplet an electrified liquid jet is formed. The jet is then elongated and whipped continuously by electrostatic repulsion (*bending instability*), describing a chaotic spiraling motion on its way to the collecting electrode. Although the process may appear

T.A. Kowalewski, S. Barral and T. Kowalczyk
IPPT-PAN, Swietokrzyska 21, Warsaw, Poland; e-mail: {tkowale,sbarral,tkowalcz}@ippt.gov.pl

simple the achievement of stable operation is not an easy task. Properties that are known to significantly affect the electrospinning process are the polymer molecular weight, the molecular-weight distribution, the architecture (branched, linear, etc.) of the polymer, as well as the rheological and electrical properties of the solution (viscosity, conductivity, surface tension, etc.). In addition, the operating conditions such as electric potential, flow rate, distance from the needle tip to the collection plate, ambient parameters (temperature, humidity), and geometry of the collecting target play a crucial role in controlling the electrospinning characteristics [1, 17, 23, 24]. Because each material demands a different optimization procedure, the development of theoretical and numerical models of electrospinning appears thus highly desirable.

The physical and mathematical description of the electrospinning process remains, however, a distant target. Despite several parametric studies performed in various experimental configurations [1, 11, 23] it appears difficult to formulate consistent scaling laws for electrospinning. The influence of the electric field and of the solution conductivity on the fibers quality was exhaustively investigated by Arayanarakul et al. [1], who concluded that higher polymer solution conductivity improves the spinning process but has only a marginal impact on the fiber size. Broadly speaking, higher applied electric potential, higher electric conductivity and viscosity of the polymer solution appear to improve fiber uniformity. Although the great role played by the electric field and the solution conductivity is conform to the intuition, experiments performed with similar configurations but different polymer solutions exhibit at times opposite relationships [1, 17]. The validation of theoretical models with experimental data is thus far from trivial [22], and it has proved so far impossible to relate actual fiber morphology to the predicted characteristics [8].

The early stage of electrospun jets has been investigated in several one-dimensional theoretical and numerical works [6, 9, 10, 13, 21], which have emphasized the importance of viscoelastic rheology. By contrast, very few studies have considered the unstable part of the jet, in part because of the difficulties inherent to its three-dimensional and unsteady character. Hohman et al. [13] have derived a linear stability theory aimed at predicting the onset of a bending mode in a straight jet, but its relevance to the actual phenomenon remains difficult to assess. A qualitative description of this instability has been given by Yarín et al. [24], using a simple discrete model consisting of point charges connected by dumbbell elements. The latter model appears to provide a reasonable explanation for the spiraling motion of the jet, but suffers from mathematical inconsistencies incurred by the discretization of the fiber into point-charges. Although this problem was remedied by accounting for the actual electrostatic form factors between two interacting sections of a charged fiber [17], electrostatic interactions have usually been accounted for *via* strong approximations [9, 10, 13]. One serious concern relates to the evaluation of short-range interactions, which in the case of standard discrete integration methods require very dense grids due to the large contribution of short-range electrostatic interactions within distances of the order of the fiber radius [14, 17]. The fiber radius being about 10^3 – 10^5 times smaller than the macroscopic scales of interest, it appears most desirable to devise a discrete model that exploits the slenderness of

the fiber to evaluate short-range interactions in an efficient manner. Likewise, the computation of long-range electrostatic interactions can easily become intractable due to the $\mathcal{O}(n^2)$ operation count for a pairwise evaluation of interactions between n elements. A third issue with current numerical models is the assumption of a static external electric field, whereas in reality the external field is modulated by the net space charge of the fiber so as to keep constant the potential over the electrodes. This latter issue can be effectively addressed by use of a boundary element method (BEM). In essence, the boundary element method is a statement of the electrostatic problem (Poisson equation) in terms of boundary integrals; as such, it involves only the discretization of boundary surfaces, which in our case would be the electrode surfaces and the outer shell of the fiber. Although BEM-based models have been investigated in the context of electrospinning [5, 14, 18, 25], no attempt has been made to cure the aforementioned inefficient evaluation of short-range and long-range interactions. An efficient handling of long-range interactions would, however, greatly benefit to both electrospinning and electrospinning simulations. For this, a variety of mesh-based and particle-based methods exist that can theoretically achieve $\mathcal{O}(n \log n)$ operation count, or even $\mathcal{O}(n)$ for the fast multipole method (FMM).

Particle-based methods are clearly at an advantage in the problem at hand, where the computation domain is three-dimensional but is only sparsely populated by a one-dimensional object (the fiber). Most fast particle-based algorithms are based on either treecode hierarchical algorithms [3] or on the FMM [12]. In either cases, distant particles are clustered and approximated as a truncated multipole expansion (of fixed order in the case of the treecode method, and of adaptive order in the FMM). The treecode algorithm considers particle-cluster interactions and achieves $\mathcal{O}(n \log n)$ complexity, while FMM considers cluster-cluster interactions and can compute forces with $\mathcal{O}(n)$ complexity. At low n , however, and when the required accuracy on the computed forces is low, the treecode is usually found to outperform FMM due to a much smaller prefactor. Furthermore, the theoretical advantage of the $\mathcal{O}(n)$ force evaluation of the FMM is somewhat mitigated by the fact that for non-uniform spatial distribution of particles – such as a fiber in 3D space – the charge clusterization step still requires $\mathcal{O}(n \log n)$ operations. Last and foremost, the treecode algorithm is simpler to implement and parallelize. It is worth noting that treecode accelerated BEMs have been recently investigated in other contexts, such as plasma physics [7].

2 Experiment

Electrospinning was performed inside a custom-made polycarbonate chamber of approximately 1 cubic meter volume. The spinneret consists of a 2 mm long grounded syringe needle of internal diameter 0.35 mm, mounted vertically on an electrically insulated stand placed 15 cm above the collecting electrode. The spinneret needle was positively biased with a high voltage power supply. A flat copper grid (310 mm \times 240 mm) with a small cage (75 mm \times 80 mm \times 50 mm) was used as ground

electrode, as described in previous reports [16, 17]. The voltage applied between the spinneret and the ground electrode was varied from 1 kV up to 30 kV. The capillary needle was connected through PTFE tubing to a plastic syringe filled with the spinning solution. A constant volume flow rate was maintained using the syringe pump. In our study, a 3% solution of poly(ethylene oxide) (PEO) of molecular weight 400 kDa in 40% ethyl alcohol/water mixture was used to analyze electrospinning process. The effect of solution electrical conductivity was investigated with three inorganic salts (NaCl, LiCl, NH₄Cl) individually dissolved in the PEO solution to attain molar salt concentration in the range 0.001–0.02 M, which corresponds to a 15-fold variation of the solution conductivity.

The electrospinning process was observed using high speed camera (hs1200.pco) and analyzed by evaluating the geometry of the fiber coils created by the electrified polymer jet. The spiral envelope angle, θ , and the length of the straight jet segment, L , were obtained from the high-speed camera images and their dependence on the applied voltage and solution composition was evaluated and correlated with microscopic images of the electrospun nanofibers.

The pure PEO solution used in the experiments exhibits a bending instability threshold at about 3kV. Farther increase of the voltage elongates the straight part of the jet and leads to the development of relatively stable, large amplitude looping. The straight part increases from about 0.5 cm to over 2.5 cm. The looping cone initially increased with the voltage but above 5kV the spiral envelope angle systematically decreased. It is in agreement with our previous findings [17]. This general trend usually did not change after increasing the electrical conductivity of the solution (compare Table 1). A similar behavior of the jet could be observed for nearly all investigated PEO-inorganic salt solutions, i.e. the straight portion of the jet increased and the looping cone decreased with the voltage. However, increased salt concentration (and hence solution conductivity) only slightly decreased the cone angle θ for two salts NaCl and NH₄Cl, whereas the opposite behavior was observed for LiCl. The jet straight part L increased with the salt concentration only for NaCl, whereas it decreased for the two other salts. Relatively small changes of the jet spiralling geometry may suggest similar elongation rate of the fiber. In fact, images of collected fibers analysed under optical and TEM microscopes could not give any clear evidence that solution conductivity changes fiber size or morphology. Dispersion of the collected data underline complexity of the problem. Increasing solution conductivity by salt additives likely modifies other polymer properties such as surface tension, viscosity, and rheology. However, according to the data collected by Arayanarakul et al. [1] and in regard to the range of salt concentration used, only a slight decrease of the surface tension (from 31 to about 28 mN/m) and viscosity (from 206 to 190 mPa/s) can be expected. Hence, it is difficult to draw definite conclusions on the effects of solution conductivity, i.e. charge density carried by the fiber.

Table 1 Variation of jet straight part L and cone angle θ for different salt concentrations c (and corresponding conductivity K) and applied voltage U_g ; data for 3% PEO water/alcohol solution at 25°C.

#	salt	c [M] K [$\mu\text{S/cm}$]	U_g [kV]	θ [grad]	L [mm]
1	–	0.0 17.1	3	85	7.1
			5	112	23.1
			10	71.3	25.2
			15	63.3	17.4
			20	58.7	11.8
2	NaCl	0.01 399.5	10	86.7	26.5
			15	62.7	38.0
			20	52.7	39.7
3	NaCl	0.02 741.3	10	61.7	24.6
			15	59.0	34.6
			20	50.0	42.5
4	LiCl	0.01 280.6	10	70.3	34.2
			15	48.3	40.2
			20	39.3	46.6
5	LiCl	0.02 551.9	10	71.7	22.8
			15	63.3	10.5
			20	69.3	18.0
6	NH ₄ Cl	0.01 457.8	10	75.7	32.1
			15	64.3	32.7
			20	59.0	33.8
7	NH ₄ Cl	0.02 906.1	10	84.0	24.0
			15	71.7	30.5
			20	60.0	31.2

3 Model

3.1 Governing Equations

The model is, essentially, a time-dependent three-dimensional generalization of known slender models [6, 9, 10, 13], with the following differences:

- (i) the electric field induced by the generator and by the charges on the fiber is explicitly resolved, instead of being approximated from local parameters [6, 9, 10].
- (ii) electrical conductivity is neglected. Indeed, the convection of surface charges is believed to strongly overcome bulk conduction at locations distant from the Taylor cone by a few fiber radii [6]; since we are mostly interested in the description of the bending instability, this assumption appears reasonable.

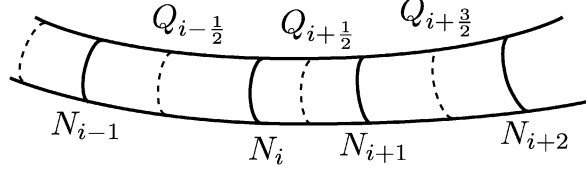


Fig. 1 Fiber discretized into finite length elements $Q_{k+1/2}$ with collocation nodes N_k localized at the element interfaces.

(iii) for the sake of simplicity, polarization effects are neglected.

(iv) the polymer is considered a viscoelastic Maxwell fluid, as in [20].

Evaporation has been systematically neglected in the literature, except in [24] where an ad-hoc evaporation model was used. Following Fridrikh et al. [11], we shall also neglect evaporation even in the whipping part of the jet, by arguing that it occurs mostly after the fiber has been maximally stretched. The mass conservation equation accordingly reads

$$\frac{\partial a^2}{\partial t} + \frac{\partial(va^2)}{\partial \xi} = 0, \quad (1)$$

where a is the fiber radius, v is the velocity of the fiber and ξ is the arc length along the fiber.

The force balance per unit of fiber length reads in turn

$$\rho\pi a^2 \ddot{\mathbf{x}} = \frac{\partial(\pi a^2 \hat{\boldsymbol{\tau}} + \pi \gamma a \hat{\mathbf{t}})}{\partial \xi} + \lambda \mathbf{E}, \quad (2)$$

where ρ is the mass density, $\ddot{\mathbf{x}}$ is the acceleration vector, γ is the surface tension coefficient, $\hat{\mathbf{t}}$ is the local unit vector tangent to the fiber, λ is the linear charge density, $\bar{\epsilon}$ is the dielectric constant of the medium (air), \mathbf{E} is the electric field and $\boldsymbol{\tau}$ is the viscoelastic stress. The stress is given by a Maxwell viscoelastic constitutive equation:

$$\dot{\boldsymbol{\tau}} = G \left(\boldsymbol{\varepsilon} - \frac{\boldsymbol{\tau}}{\mu} \right), \quad (3)$$

where G is the elastic modulus, μ the fluid viscosity and $\boldsymbol{\varepsilon}$ the Lagrangian axial strain

$$\boldsymbol{\varepsilon} \equiv \frac{\partial \dot{\mathbf{x}}}{\partial \xi} \cdot \hat{\mathbf{t}}. \quad (4)$$

3.2 Discretization and Electrostatic Solver

A Lagrangian discrete model is used. The fiber is first decomposed into discrete charged elements $Q_{i+1/2}$, the length of which is typically much greater than the

fiber radius, but smaller than other characteristic lengths of interest (such as the curvature radius). The equation of motion (2) is then resolved at the interfaces of each element (collocation nodes N_i , see Figure 1), where all forces are priorly evaluated. After displacements have been calculated, the radius in the central sections of elements $Q_{i+1/2}$, is straightforwardly obtained since the volume of each element is conserved. Likewise, the linear charge density in the center section is computed by assuming that the total charge of each element is conserved. The scheme is thus intrinsically mass and charge conserving (but is not momentum conserving).

The forces at each collocation node are computed from the following discrete form of Eq. 2:

$$\begin{aligned} \ddot{\mathbf{x}}_i = & \frac{1}{\rho\pi a_i^2} \frac{\pi(a^2\tau)_{i+1/2} - \pi(a^2\tau)_{i-1/2} + \pi\gamma(a_{i+1/2} - a_{i-1/2})}{\frac{1}{2}(|\mathbf{x}_i - \mathbf{x}_{i-1}| + |\mathbf{x}_{i+1} - \mathbf{x}_i|)} \hat{\mathbf{t}}_i \\ & + \frac{1}{\rho} \left(\tau_i + \frac{\gamma}{a_i} \right) \kappa_i \hat{\mathbf{n}}_i + \lambda_i \mathbf{E}_i. \end{aligned} \quad (5)$$

The values a_i , τ_i , λ_i required at the collocation nodes are linearly interpolated from those computed in the central section of the neighboring elements. The local tangent vector $\hat{\mathbf{t}}_i$ and curvature vector $\kappa_i \hat{\mathbf{n}}_i$ are computed from the approximate osculating circle defined by (N_{i-1}, N_i, N_{i+1}) .

Time integration is realized with a classical leapfrog scheme, which presents the advantage over other second order schemes by requiring only one evaluation of force term per time step:

$$\dot{\mathbf{x}}_i^{n+1/2} = \dot{\mathbf{x}}_i^{n-1/2} + \ddot{\mathbf{x}}_i^n \Delta t, \quad (6)$$

$$\mathbf{x}_i^{n+1} = \mathbf{x}_i^n + \dot{\mathbf{x}}_i^{n+1/2} \Delta t, \quad (7)$$

where upper indices refer to time. Eq. (5) shows that the accelerations $\ddot{\mathbf{x}}_i^n$ can be explicitly obtained from the positions \mathbf{x}_i^n at the same instant, except for the contribution of the viscoelastic stress as the latter integrates a memory effect. A discretization of the stress equation (3) which preserves second order time accuracy of the scheme can nonetheless be found using

$$\frac{\sigma_{i+1/2}^{n+1} - \sigma_{i+1/2}^n}{\Delta t} = G \varepsilon_{i+1/2}^{n+1/2} - \frac{1}{2\mu} (\sigma_{i+1/2}^n + \sigma_{i+1/2}^{n+1}), \quad (8)$$

$$\varepsilon_{i+1/2}^{n+1/2} = \frac{1}{2} \frac{(\mathbf{x}_{i+1}^n - \mathbf{x}_i^n + \mathbf{x}_{i+1}^{n+1} - \mathbf{x}_i^{n+1})(\dot{\mathbf{x}}_{i+1}^{n+1/2} - \dot{\mathbf{x}}_i^{n+1/2})}{(\mathbf{x}_{i+1}^n - \mathbf{x}_i^n + \mathbf{x}_{i+1}^{n+1} - \mathbf{x}_i^{n+1})^2}, \quad (9)$$

since Eq. (8) is easily recast into a time-explicit expression for $\sigma_{i+1/2}^{n+1}$.

Dynamic refinement is used in simulations to maintain the size of elements below a prescribed characteristic length ℓ_{\max} ; whenever an element is elongated beyond ℓ_{\max} , it is split into two elements, each containing half the charge and mass of the initial element.

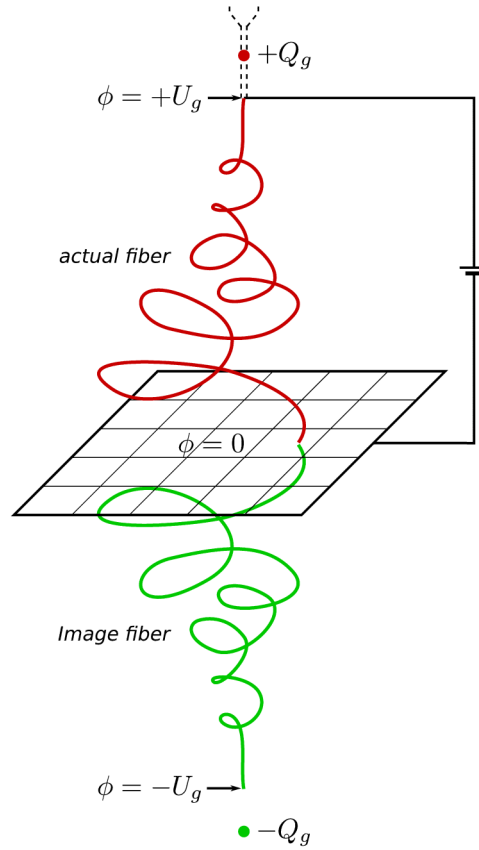


Fig. 2 Idealized electrostatic configuration: the potential is prescribed between the tip of the needle and a grounded infinite plane. The needle electrode is modeled as a point electrode, the charge of which is computed such as to always maintain the prescribed potential at the needle tip. Image charges are used to implement the potential condition $\phi = 0$ on the infinite plane.

The needle and the grounded collector are idealized by a point-charge/plate capacitor configuration, whereas the point-charge is meant to qualitatively reproduce the field lines concentration that exists close to the needle. The potential is prescribed between the location at which the fluid is introduced (the tip of the needle) and the infinite plane where the fiber is collected. A practical way to resolve the electrostatic field in such a configuration is the method of images (see Figure 2), whereas fictive mirror charges are placed symmetrically to the ground plane. The charge of the capacitor is computed at any instant to satisfy the prescribed potential $\phi = U_g$ at the inlet.

The electrostatic field induced by the fiber can be computed by considering that the charges are distributed on the centerline of the fiber, as demonstrated by Homann et al. [13]. This alleviates the need for complex form factors, as used previously by

the authors and others [5, 14, 17]. Even so, the computation of electrostatic interactions between the discrete charge elements Q_i remains a complex problem. First, if a typical BEM implementation with pairwise evaluation of electrostatic interactions is used, the problem scales as $\mathcal{O}(n^2)$ where n is the number of discrete elements. A more efficient, albeit more complex method is the hierarchical force calculation algorithm (*treecode*) [3], which complexity scales as $\mathcal{O}(n \log n)$. Charge elements are in that case recursively clustered and the monopole coefficients (charge and center of charge) of the clusters are computed. The field at a location N_i is then computed by considering only the largest clusters which are sufficiently well separated [12], that is, for which the distance $d_{i,C}$ between the collocation node N_i and the charge center of the cluster satisfies

$$\frac{R_C}{d_{i,C}} < \alpha, \quad (10)$$

where $\alpha < 1$ determines the accuracy of the force evaluation and R_C is the radius of a sphere containing all the charges of the cluster. Value $\alpha = 0.8$ was used in our computations.

A typical implementation of the treecode or FMM involves the recursive decomposition of the space domain into cubic cells, where each parent cell contains up to 8 children cubic cells, until each cell contains a single charge. Hence, the root of the oct-tree contains all charges of the domain and its leaves contain the charges. In our case, however, it is possible to create a hierarchized tree at a much lower costs, since the fiber approximately organizes the charges by nearest neighbors. At each time step, a binary tree is thus constituted by recursively grouping neighbors two by two, as illustrated by Figure 3, calculating at each level the smallest enclosing spheres that contain the cluster pairs. The root of the tree is a sphere that contains all charges, and its leaves are the elements $Q_{i+1/2}$. Unlike the classical treecode clusterization algorithm, this method creates a fully balanced tree and consequently easily lends itself to parallelization.

To evaluate the field at a given collocation node, condition (10) is first tested on the root cluster, and, whenever it fails, on the two subclusters recursively until clusters which are sufficiently separated are found. If a leaf element is reached which does not satisfy condition (10), the interaction is considered a close interaction and near-field expressions must be used instead of the monopole approximation. Otherwise, far field expression are used based on the monopole approximation of the cluster. It must be underlined, however, that since charges are assumed to lay on the centerline but induce a field on the outer shell of the fiber, one must account for a small correction to the classical potential and Coulomb's law:

$$\phi_{C \rightarrow i} = \frac{1}{4\pi\epsilon} \frac{q_C}{\sqrt{d_{i,C}^2 + a_i^2}}, \quad (11)$$

$$\mathbf{E}_{C \rightarrow i} = \frac{1}{4\pi\epsilon} \frac{q_C}{d_{i,C}^2 + a_i^2} \mathbf{u}_{C \rightarrow i}, \quad (12)$$

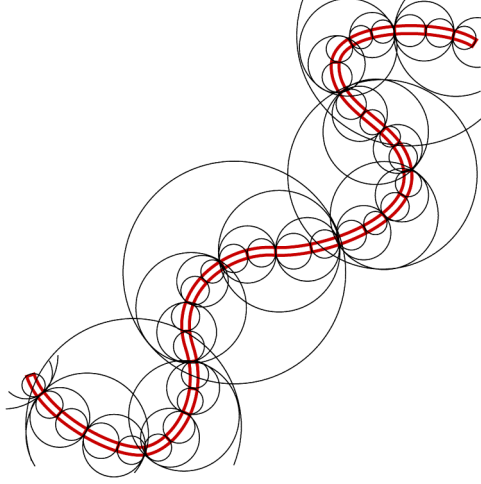


Fig. 3 Illustration of the clustering method used in our treecode implementation: neighbor charges are recursively grouped two-by-two and the smallest enclosing spheres are calculated at each clustering level, until all charges are contained in a binary tree which root is a sphere that contains all charges.

which is to be contrasted with the laws in $1/d$ and $1/d^2$ for monopole-monopole interaction. In the above, q stands for the total charge of the cluster and \mathbf{u} for the unit vector pointing to the collocation node. Obviously, the above formulae are exact only for a monopole that lies along the axis of the ring where the field is evaluated. However, the slenderness of the fiber implies that nearby charges are located close to the axis; therefore, this condition is violated only when the cluster is far ($d \gg a$), in which case the error made is negligible since the formula reduces to Coulomb's law (which is appropriate when $d \gg a$).

As mentioned earlier, condition (10) may not be fulfilled by nearby elements. This happens in particular for elements $Q_{i-1/2}$ and $Q_{i+1/2}$, which are contiguous to node N_i . In such case, the following near-field analytical expressions are used:

$$\Phi_{C \rightarrow i} = \frac{\lambda_C}{4\pi\bar{\epsilon}} \left[\operatorname{asinh} \left(\frac{\xi_i - \xi_{C_0}}{a_i} \right) - \operatorname{asinh} \left(\frac{\xi_i - \xi_{C_1}}{a_i} \right) \right], \quad (13)$$

$$\begin{aligned} (\mathbf{E} \cdot \hat{\mathbf{t}})_{C \rightarrow i} = & \frac{\lambda_C}{4\pi a_i \bar{\epsilon}} \left[\frac{1 + \frac{\xi_{C_1} - \xi_{C_0} \lambda'_C}{2 \lambda_C}}{\sqrt{1 + \left(\frac{\xi_i - \xi_{C_1}}{a_i} \right)^2}} - \frac{1 - \frac{\xi_{C_1} - \xi_{C_0} \lambda'_C}{2 \lambda_C}}{\sqrt{1 + \left(\frac{\xi_i - \xi_{C_0}}{a_i} \right)^2}} \right] \\ & + \frac{d\lambda_C}{4\pi\bar{\epsilon} d\xi} \left[\operatorname{asinh} \left(\frac{\xi_i - \xi_{C_1}}{a_i} \right) - \operatorname{asinh} \left(\frac{\xi_i - \xi_{C_0}}{a_i} \right) \right], \quad (14) \end{aligned}$$

$$\begin{aligned}
(\mathbf{E} \cdot \hat{\mathbf{n}})_{C \rightarrow i} = & \frac{\kappa \lambda_C}{4\pi \bar{\epsilon}} \left[\frac{\frac{\xi_i - \xi_{C_1}}{a_i}}{\sqrt{1 + \left(\frac{\xi_i - \xi_{C_1}}{a_i}\right)^2}} - \frac{\frac{\xi_i - \xi_{C_0}}{a_i}}{\sqrt{1 + \left(\frac{\xi_i - \xi_{C_0}}{a_i}\right)^2}} \right] \\
& + \frac{\kappa \lambda_C}{4\pi \bar{\epsilon}} \left[\operatorname{asinh} \left(\frac{\xi_i - \xi_{C_0}}{a_i} \right) - \operatorname{asinh} \left(\frac{\xi_i - \xi_{C_1}}{a_i} \right) \right], \quad (15)
\end{aligned}$$

which are leading order approximation for the potential and field generated by a slender, curved line charge on a neighboring ring. Here, λ_C is the linear charge density of the line charge, ξ_i the curvilinear location of the location where the field and potential are evaluated, ξ_{C_0} and ξ_{C_1} the locations of the end points of the line charge and κ the curvature of the fiber.

Boundary conditions implemented at the inlet (tip of the needle) prescribe the volume flow rate Q_v , the surface charge density σ_0 and the initial fiber radius a_0 . The initial stress is set to zero. It must be noted, however, that boundary conditions are notoriously difficult to implement in a consistent way in electrospinning models. This is even more true in the present case where electrical conductivity is neglected and where the charge density is not computed self-consistently. We observe a clear influence of both the boundary conditions and the discretization parameters at the inlet where strong gradients take place, which clearly challenge the assumption of slenderness. Additional investigations will be required in the future to derive boundary conditions that avoid such singularities.

A small random perturbation to the position of each element introduced at the inlet is imposed, so as to initiate the bending instability. The magnitude of this perturbation has no notable influence on the simulation results, provided that it is small enough.

3.3 Simulation Results

Behavior of the code was tested using parameters typical for the experiment. Several test runs performed confirmed general ability of the code to replicate our previous findings [17], i.e. increased electrical potential, solution viscosity and elastic modulus decreased jet sweeping amplitude, effectively seen as decreasing of the spiral cone. Here, we show an example of the simulation results obtained by varying fiber charge density and the voltage. Although it is not possible to directly integrate the liquid electrical conductivity into the model at this point, we shall assume that the conductivity mainly affects the electrical current and thus the charge density carried by the fiber. The simulations shown were performed for the following process parameters: surface tension $\gamma = 0.02$ N/m, elastic modulus $G = 10$ kPa, viscosity $\mu = 10$ Pa-s, mass density $\rho = 1000$ kg/m³, volume flow rate $Q_v = 1$ mm³/s, initial fiber radius $a_0 = 150$ μ m, distance between needle tip and collector 20 cm, and distance between point charge and needle tip 1 cm. Typical jet paths are plotted

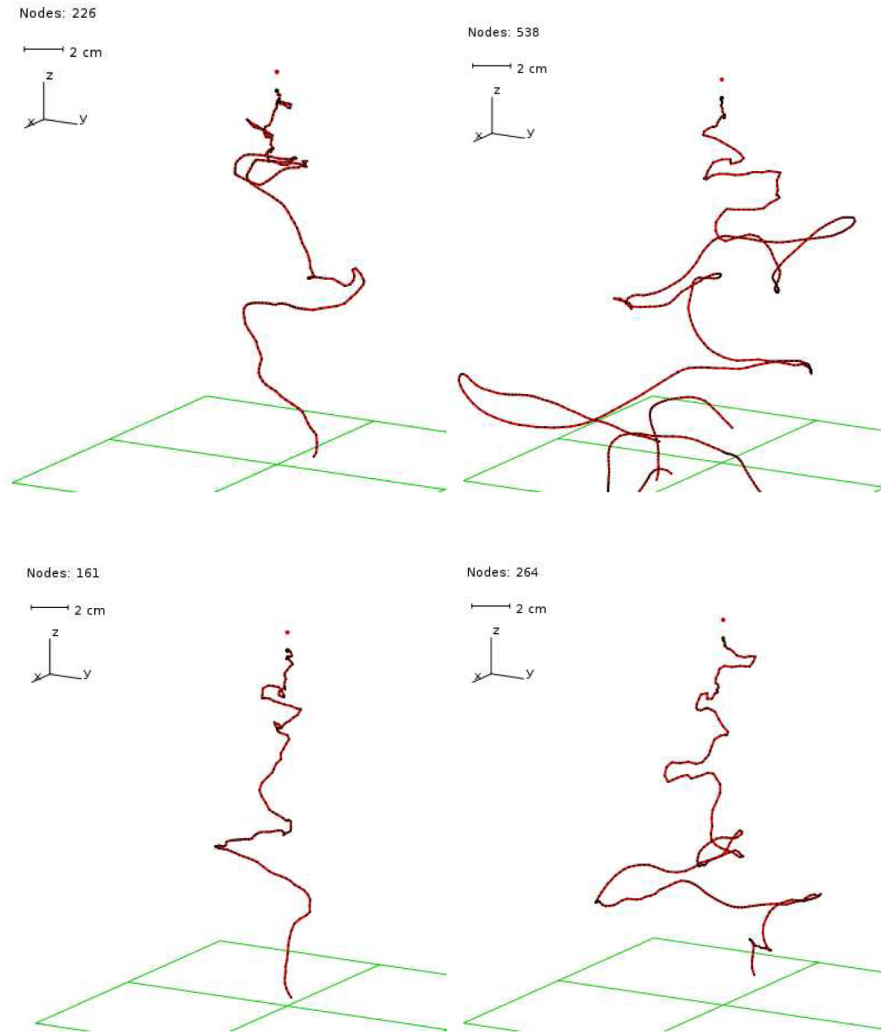


Fig. 4 Simulated jet paths at $U_g = 10$ kV (upper row) and 15 kV (bottom row), for two charge densities 10 C/m^3 (left) and 20 C/m^3 (right).

on Figure 4. As we may find the model is unable to predict initial straight part of the jet. Hence we may only compare geometry of the spiral cone.

We may conclude that higher charge density evidently increases amplitude of the jet sweeps. It is only partly consistent with the experimental findings (compare Table 1), where the cone angle first increases for lower salt concentrations but again decreases for higher values. Obviously, secondary effects due to the salt-polymer interactions may play a role for higher concentrations.

4 Conclusions

In this paper we have investigated dynamics of electrospun fibers within the slender-body approximation proposing numerically consistent model based on hierarchical charge clustering. A versatile boundary value method is implemented to enforce fixed-potential boundary conditions, allowing realistic electrode configurations to be investigated. The model is tested against experiments performed for different polymer-salt solutions. Due to the several experimental and theoretical limitations the model outcome predicts only qualitatively observed experimentally dependence of the jet geometry on the solution conductivity. Further investigations are necessary to elucidate sources of inconsistencies between the experimental findings and the modeling.

Acknowledgements This work was supported by the Polish Ministry of Science Grant No. N508 031 31/1740. The authors thank Diana Lamparska for her invaluable help in experimental work.

References

1. Arayanarakul, K., Choktaweasap, N., Aht-ong, D., Meechaisue, C., Supaphol, P.: Effects of poly(ethylene glycol), inorganic salt, sodium dodecyl sulfate, and solvent system on electrospinning of poly(ethylene oxide). *Macromol. Mater. Eng.* **291**, 581 (2006).
2. Arumuganathar, S., Jayashinghe, S.N.: Living scaffolds (specialized and unspecialized) for regenerative and therapeutic medicine. *Biomacromolecules* **9**, 759 (2008).
3. Barnes, J., Hut, P.: A hierarchical $O(N \log N)$ force-calculation algorithm. *Nature* **324**, 446 (1986).
4. Bhattarai, S.R., Bhattarai, N., Yi, H.K., Hwang, P.H., Kim, H.Y.: Novel biodegradable electrospun membrane: Scaffold for tissue engineering. *Biomaterials* **25**, 2595 (2004).
5. Carretero-Benignos, J.A.: Numerical simulation of a single emitter colloid thruster in the pure droplet cone-jet mode. Ph.D. thesis, Massachusetts Institute of Technology (2005).
6. Carroll, C.P., Joo, Y.L.: Electrospinning of viscoelastic Boger fluids: Modeling and experiments. *Phys. Fluids* **18**, 053102 (2006).
7. Christlieb, A.J., Krasny, R., Verboncoeur, J.P., Emhoff, J.W., Boyd, I.D.: Grid-free plasma simulation techniques. *IEEE. Trans. Plasma Sci.* **34**, 149 (2006).
8. Dayal, P., Kyu, T.: Dynamics and morphology development in electrospun fibers driven by concentration sweeps. *Phys. Fluids* **19**, 1011061 (2007).
9. Feng, J.J.: The stretching of an electrified non-Newtonian jet: A model for electrospinning. *Phys. Fluids* **14**, 3912 (2002).
10. Feng, J.J.: Stretching of a straight electrically charged viscoelastic jet. *J. Non-Newtonian Fluid Mech.* **116**, 55 (2003).
11. Fridrikh, S.V., Yu, J.H., Brenner, M.P., Rutledge, G.C.: Controlling the fiber diameter during electrospinning. *Phys. Rev. Lett.* **90**, 144502 (2003).
12. Greengard, L., Rokhlin, V.: A fast algorithm for particle simulations. *J. Comput. Phys.* **73**, 325 (1987).
13. Hohman, M.M., Shin, M., Rutledge, G., Brenner, M.P.: Electrospinning and electrically forced jets. I. Stability theory. *Phys. Fluids* **13**, 2201 (2001).
14. Khayms, V.: Advanced propulsion for microsatellites. Ph.D. thesis, Massachusetts Institute of Technology (2000).

15. Ko, F.K., El-Aufy, A., Lam, H.: *Wearable Electronics and Photonics*, chap. Electrostatically Generated Nanofibres for Wearable Electronics, pp. 13–40. Woodhead Publishing Ltd., Cambridge, UK (2005).
16. Kowalczyk, T., Nowicka, A., Elbaum, D., Kowalewski, T.A.: Electrospinning of bovine serum albumin. Optimization and use for the production of biosensors. *Biomacromolecules* (2008) (to appear).
17. Kowalewski, T.A., Blonski, S., Barral, S.: Experiments and modelling of electrospinning process. *Bull. Polish Acad. Sci.* **53**, 385 (2005).
18. Lopez-Herrera, J.M., Ganan-Calvo, A.M., Perez-Saborid, M.: One-dimensional simulation of the breakup of capillary jets of conducting liquids. Application to E.H.D spraying. *J. Aerosol Sci.* **30**, 895 (1999).
19. Luu, Y.K., Kim, K., Hsiao, B., Chu, B., Hadjiargyrou, M.: Development of a nanostructured DNA delivery scaffold via electrospinning of PLGA and PLAPEG block copolymers. *J. Control. Release* **89**, 341 (2003).
20. Reneker, D.H., Yarin, A.L., Fong, H., Koombhongse, S.: Bending instability of electrically charged liquid jets of polymer solutions in electrospinning. *J. Appl. Phys.* **87**, 4531 (2000).
21. Spivak, A.F., Dzenis, Y.A.: Asymptotic decay of radius of a weakly conductive viscous jet in an external electric field. *Appl. Phys. Lett.* **73**, 3067 (1998).
22. Thompson, C.J., Chase, G.G., Yarin, A.L., Reneker, D.H.: Effects of parameters on nanofiber diameter determined from electrospinning model. *Polymer* **48**, 6913 (2007).
23. Yang, Y., Jia, Z., Li, Q., Guan, Z.: Experimental investigation of the governing parameters in the electrospinning of polyethylene oxide solution. *IEEE Trans. Dielectr. Electr. Insul.* **13**, 580 (2006).
24. Yarin, A.L., Koombhongse, S., Reneker, D.H.: Bending instability in electrospinning of nanofibers. *J. Appl. Phys.* **89**, 3018 (2001).
25. Yoon, S.S., Heister, S.D., Epperson, J.T., Sojka, P.E.: Modeling multi-jet mode electrostatic atomization using boundary element methods. *J. Electrostat.* **50**, 91 (2001).